



**HAL**  
open science

## Metal-silicate mixing by large Earth-forming impacts

Maylis Landeau, Renaud Deguen, Dominic Phillips, Jerome A Neufeld, Victor Lherm, Stuart B Dalziel

► **To cite this version:**

Maylis Landeau, Renaud Deguen, Dominic Phillips, Jerome A Neufeld, Victor Lherm, et al.. Metal-silicate mixing by large Earth-forming impacts. *Earth and Planetary Science Letters*, 2021, 564, pp.116888. 10.1016/j.epsl.2021.116888 . hal-03271232

**HAL Id: hal-03271232**

**<https://hal.science/hal-03271232>**

Submitted on 25 Jun 2021

**HAL** is a multi-disciplinary open access archive for the deposit and dissemination of scientific research documents, whether they are published or not. The documents may come from teaching and research institutions in France or abroad, or from public or private research centers.

L'archive ouverte pluridisciplinaire **HAL**, est destinée au dépôt et à la diffusion de documents scientifiques de niveau recherche, publiés ou non, émanant des établissements d'enseignement et de recherche français ou étrangers, des laboratoires publics ou privés.

# Metal-silicate mixing by large Earth-forming impacts

Maylis Landeau<sup>a,b,\*</sup>, Renaud Deguen<sup>c</sup>, Dominic Phillips<sup>b</sup>, Jerome A. Neufeld<sup>b,d,e</sup>, Victor Lherm<sup>f</sup>,  
Stuart B. Dalziel<sup>b</sup>

<sup>a</sup>Université de Paris, Institut de Physique du Globe de Paris, CNRS, 75005 Paris, France

<sup>b</sup>Department of Applied Mathematics and Theoretical Physics, University of Cambridge, Wilberforce Road, Cambridge CB3 0WA,  
United Kingdom

<sup>c</sup>ISTerre, CNRS, Université Grenoble Alpes, 38058 Grenoble, France

<sup>d</sup>Department of Earth Sciences, University of Cambridge, Cambridge CB3 0EZ, United Kingdom

<sup>e</sup>BP Institute, University of Cambridge, Cambridge CB3 0EZ, United Kingdom

<sup>f</sup>Laboratoire de Géologie de Lyon, Université Lyon 1, 69622 Villeurbanne, France

---

## Abstract

Geochemical and isotopic observations constrain the timing, temperature and pressure of Earth's formation. However, to fully interpret these observations, we must know the degree of mixing and equilibration between metal and silicates following the collisions that formed the Earth. Recent fluid dynamical experiments provide initial estimates of this mixing, but they entirely neglect the inertia of planet-building impactors. Here we use laboratory experiments on the impact of a dense liquid volume into a lighter liquid pool to establish scaling laws for mixing as a function of the impactor speed, size, density and the local gravity. Our experiments reproduce the cratering process observed in impact simulations. They also produce turbulence down to small scales, approaching the dynamical regime of planetary impacts. In each experiment, we observe an early impact-dominated stage, which includes the formation of a crater, its collapse into an upward jet, and the collapse of the jet. At later times, we observe the downward propagation of a buoyant thermal. We quantify the contribution to mixing from both the impact and subsequent thermal stage. Our experimental results, together with our theoretical calculations, indicate that the collapse of the jet produces much of the impact-induced mixing. We find that the ratio between the jet inertia and the impactor buoyancy controls mixing. Applied to Earth's formation, we predict full chemical equilibration for impactors less than 100 km in diameter, but only partial equilibration for Moon-forming giant impacts. With our new scalings that account for the impactor inertia, the mass transfer between metal and silicates is up to twenty times larger than previous estimates. This reduces the accretion timescale, deduced from isotopic data, by up to a factor of ten and the equilibration pressure, deduced from siderophile elements, by up to a factor of two.

**Keywords:** Planetary impacts, giant impacts, Earth's differentiation, metal-silicate equilibration, mixing, liquid impacts, turbulent thermal.

## 34 1. Introduction

35 The Earth formed 4.6 billion years ago (Patterson et al., 1955) by successive planetary collisions. During  
36 this process, the metallic core and the silicate mantle differentiated and acquired their initial temperature and  
37 composition. These initial conditions shaped the present-day structure and dynamics of our planet. They  
38 determined the beginning of the geodynamo (Badro et al., 2018), the initiation of plate tectonics (Bercovici  
39 and Ricard, 2014) and the nucleation of the inner core (Olson et al., 2015).

40 Geochemical observations tell us about Earth's differentiation. Isotopic ratios and extinct radioactivity  
41 indicate that the core formed in about 30 Myr (Kleine et al., 2002). During differentiation, chemical species  
42 partition into metal and silicates depending on pressure and temperature. Mantle abundances in siderophile  
43 elements suggest the separation of metal and silicates at a high temperature of 3000 – 3500 K and depths of  
44 1000 – 1500 km (Siebert et al., 2012; Fischer et al., 2015).

45 However, these estimates all assume that metal was in thermodynamic equilibrium with the entire mantle  
46 when it segregated into the core. Recent models relax this assumption, allowing for equilibration of only  
47 fractions of the core and mantle. With these assumptions, the duration of core formation, deduced from  
48 isotopic ratios, becomes indeterminate, varying from 30 Myr to 100 Myr or more (Rudge et al., 2010).  
49 Similarly, the equilibrium pressure deduced from siderophile abundances extends to that of the core-mantle  
50 boundary when allowing for partial equilibration (Fischer et al., 2017). An accurate assessment of chemical  
51 transfers is therefore needed to fully interpret geochemical observations. These transfers depend on the  
52 efficiency of mixing between metal and silicates, and hence on the fluid dynamics of Earth's differentiation  
53 (Rubie et al., 2003).

54 Models of planetary formation suggest that much of Earth's mass accreted by collisions between plane-  
55 tary embryos composed of a metallic core and a silicate mantle (Chambers, 2004; Ricard et al., 2009). Each  
56 impact produced shock-waves that melted the colliding embryos, releasing the liquid core of the impactor  
57 in a fully-molten magma ocean (Fig.1a) (Tonks and Melosh, 1993; Nakajima et al., 2020). The impactor  
58 core sank into this ocean and merged with the core of the target embryo. During this process, the dy-  
59 namics were highly turbulent: inertia was large compared to surface tension and viscous forces (Dahl and  
60 Stevenson, 2010; Deguen et al., 2011). Turbulence mixed the impactor core and the magma ocean down to  
61 small-scales, increasing the rate of chemical equilibration.

62 The first physical estimates of this mixing come from theoretical and numerical calculations (Rubie  
63 et al., 2003; Ichikawa et al., 2010; Ulvrova et al., 2011; Samuel, 2012; Qaddah et al., 2019; Maas et al.,  
64 2021). These suggest that, following a collision, the impactor core broke up into centimetric drops, forming  
65 a rain of metal in the magma ocean. Laboratory experiments on the fragmentation of a liquid volume find  
66 different dynamics (Landeau et al., 2014; Deguen et al., 2014). They suggest that, instead of forming a

---

\*Corresponding author  
Email address: landeau@ipgp.fr (Maylis Landeau)

67 rain, the impactor core fell in the ocean as a dense, coherent cloud that entrained silicates. This structure is  
68 called a *turbulent thermal* in fluid dynamics (Morton et al., 1956). In the thermal, the impactor metal was  
69 stretched and convolved with the entrained silicates (Lherm and Deguen, 2018). It eventually fragmented  
70 into millimetric drops at depths 4 – 8 times the radius of the impactor core (Landeau et al., 2014). By  
71 fragmenting, the impactor metal increased its surface area, thus enhancing chemical transfers. However,  
72 the impactor core equilibrated only with the silicates entrained inside the thermal, i.e. only with a fraction  
73 of the mantle. From existing theories on thermals, Deguen et al. (2014) develop a predictive model for the  
74 volume of mixed silicates and the degree of equilibration. Wacheul and Le Bars (2018) recently validate  
75 these predictions in immiscible thermals.

76 However, this picture is still incomplete. These previous investigations all neglect the inertia of the  
77 impactor and the disruption caused by the impact. This is at odds with geological observations on terrestrial  
78 craters, which indicate that the impactor was strongly dispersed within the target. These observations are  
79 particularly clear for Meteor Crater (Arizona, USA), where we find fragments of the iron meteorite that  
80 formed the crater kilometres away from the impact point (Blau et al., 1973; Vdovykin, 1973).

81 These observations raise an important, still unresolved, question: During an Earth-forming collision,  
82 was the impactor core dispersed? If it was, metal-silicate equilibration was stronger than the estimates  
83 of Deguen et al. (2014). In this work, we use fluid dynamical experiments to quantify mixing by a large  
84 planetary impact and reassess metal-silicate equilibration.

## 85 **2. Modelling planetary impacts**

86 The most widely recognised method to investigate planetary impacts is numerical modelling (Canup,  
87 2004; Čuk and Stewart, 2012; Kendall and Melosh, 2016). Kendall and Melosh (2016) use high-resolution  
88 simulations to characterise the stretching of the impactor core. They observe that, on impact, the core  
89 spreads into a thin layer over the deforming crater floor. The crater then collapses and rises as a vertical jet,  
90 stretching the core to an even greater extent. However, while the simulations of Kendall and Melosh (2016)  
91 resolve scales down to 2.5 km, the typical length scale for chemical equilibration is 1 cm (Rubie et al., 2003;  
92 Ulvrová et al., 2011).

93 Here, to model turbulent mixing down to such small scales, we use analogue laboratory experiments.  
94 We investigate liquid volumes falling in air and impacting into another miscible liquid (Fig. 1b). We  
95 quantify mixing between the released volume, representing the impactor, and the target, representing the  
96 magma ocean, as a function of the impact speed. Unlike impact simulations, these experiments are subsonic  
97 and cannot produce significant heating. In addition, our impactors are not differentiated into a core and a  
98 mantle. However, these experiments complement impact simulations by accurately constraining small-scale  
99 mixing, which is crucial in estimating metal-silicate equilibration.

100 Why would impacts between Newtonian liquids reproduce the dynamics of solid planetary impacts?



101 Collisions onto a planetary embryo larger than 2000 km in diameter produce shock waves that melt both the  
102 impactor and target (Tonks and Melosh, 1993). In addition, the pressures produced by impactors  $\gtrsim 100$  km  
103 are much larger than the strength of the solid mantle. This is the so-called *gravity regime* (Melosh, 1989).  
104 In this regime, the impactor and target behave as fluids.

105 In planetary impacts, the impactor core and the magma ocean are immiscible. This immiscibility con-  
106 trols the size of the metal fragments (Deguen et al., 2011; Wacheul and Le Bars, 2018). Here, we do not  
107 investigate this size. Instead, we focus on the overall volume of silicates entrained with metal. During a  
108 planetary impact, inertial forces are much larger than interfacial forces between metal and silicates (Deguen  
109 et al., 2011). In this regime, the rate of entrainment is identical to that observed in miscible liquids (Lan-  
110 deau et al., 2014). Metal-silicate immiscibility therefore plays no role in the entrainment; hence, we study  
111 miscible impactor and target liquids here.

112 Still, in our experiments and planetary impacts, the target and impactor are immiscible with the air. The  
113 impact of millimetric drops at an air-liquid interface is a classical, yet active, topic in fluid dynamics (Wor-  
114 thington, 1908; Ray et al., 2015). During drop impacts, viscous dissipation and surface tension with air play  
115 an important role. In contrast, both effects are small compared to gravity and inertia during large planetary  
116 impacts. To reach this inertial regime, we conduct the first impact experiments with large decimetre-sized  
117 liquid impactors.

118 Here, we first introduce the experimental setup (section 3). After a qualitative description of the impact  
119 dynamics (section 4.1), we demonstrate that our experiments replicate the cratering process observed in  
120 previous subsonic impacts (section 4.2). We derive scaling laws for the mixing between the impactor and  
121 the target (section 4.3), which we explain by scaling arguments (section 4.4). Finally, we translate our  
122 scalings into improved estimates for the degree of equilibration (section 5.2).

### 123 3. Methods

#### 124 3.1. Experimental set-up

125 Fig.1 shows the geophysical motivation and the experimental set-up. A volume of salt solution of density  
126  $\rho_i$  and radius  $R$  impacts a target liquid of density  $\rho_t$ , representing the magma ocean. The target liquid is held  
127 in an acrylic tank, with a 76 cm square planform, filled with fresh water to a depth of 50 cm. We vary the  
128 impact velocity  $U$  by varying the release height of the impactor.

129 In this study, we take  $R \gtrsim 3$  cm. We initially hold the impacting liquid in a latex balloon. We place a  
130 needle below the balloon, at less than 30 cm above the target surface. When we release the balloon, it falls  
131 onto the needle, which ruptures the latex membrane and releases a nearly spherical liquid volume.

132 We visualise the flow by back illumination through a diffusive screen. The light source, measuring 90  
133 cm  $\times$  120 cm, is a panel of red LEDs driven by a stabilised DC power supply. In order to characterise fluid  
134 mixing, we dye the impacting liquid using blue food colouring at a volumetric concentration of 0.025%. We

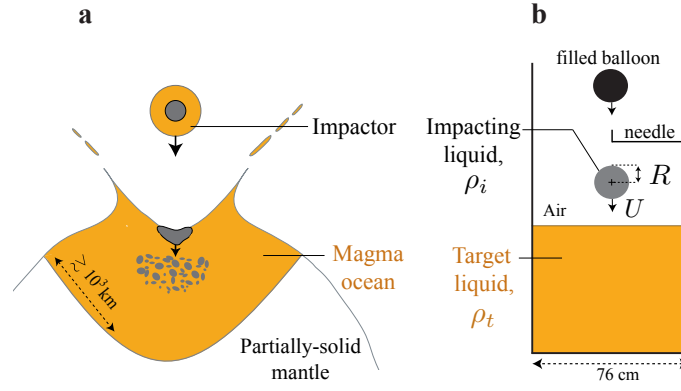


Figure 1: (a) Metal-silicate mixing by a planetary impact; the impactor core is in grey, the magma ocean in yellow and the partially-solid mantle in white. In this sketch, the magma pool is generated by the impact (Melosh, 1990; Nakajima et al., 2020). Alternatively, the magma ocean can predate the impact; it then forms a layer of uniform thickness. (b) Experimental set-up (side view). A liquid impactor of radius  $R$  and density  $\rho_i$  impacts a target liquid of density  $\rho_t < \rho_i$  at velocity  $U$ . The impacting and pool liquids are analogues for the impactor and the magma ocean, respectively.

135 also conduct a series of experiments with no dye to measure precisely the transient crater depth. The flow  
 136 is recorded with a Photron SA1.1 monochrome high-speed camera with a resolution of  $1024 \times 1024$  pixels.  
 137 We use 1000 frames per second to image the impact stage (see section 4.1) and 125 frames per second for  
 138 the slower buoyancy-induced thermal stage (as defined in section 4.1).

139 In order to vary the density of the impacting liquid, we use solutions of sodium chloride (NaCl) at  
 140 different concentrations to give densities between  $\rho_i = 998.66 \text{ kg m}^{-3}$  and  $1100.78 \text{ kg m}^{-3}$ . The target pool  
 141 density is fixed at  $\rho_t = 998.66 \text{ kg m}^{-3}$ . For each experiment we weigh the impacting liquid and measure  
 142 its density using an Anton Paar DMA 5000 density meter, from which we deduce the equivalent spherical  
 143 radius  $R$  of the impactor.

### 144 3.2. Dimensionless numbers

The following dimensionless numbers govern the dynamics in planetary impacts and in our experiments:

$$Fr = \frac{U^2}{gR}, \quad P = \frac{\rho_i - \rho_t}{\rho_t}, \quad (1)$$

$$We = \frac{\rho_i U^2 R}{\sigma_t}, \quad Re = \frac{UR}{\nu_t}, \quad M = \frac{U}{U_s}, \quad \frac{\nu_i}{\nu_t}, \quad \frac{\sigma_i}{\sigma_t}.$$

145 The impact Froude number  $Fr$  measures the importance of the impactor kinetic energy to its gravitational  
 146 energy at impact, as discussed in supplementary section S1, where  $g$  is the gravitational acceleration. The  
 147 Weber number  $We$  and the Reynolds number  $Re$  measure the importance of the impactor kinetic energy to  
 148 the interfacial energy and viscous dissipation, respectively. The ratio  $P$  is the normalised excess density  
 149 of the impactor. The Mach number  $M$  is the ratio of the impact velocity  $U$  to the speed of sound  $U_s$ ,  
 150 and  $\nu_i/\nu_t$  and  $\sigma_i/\sigma_t$  are the ratios of impactor to target kinematic viscosities and surface tensions with air,  
 151 respectively. Supplementary Table 1 compares the values of these parameters in our experiments and in the

152 large impacts of Earth’s formation.

153 During a planetary impact, the Mach number is  $M = 1-10$ . We cannot reach these supersonic conditions  
154 when releasing a liquid impactor in the laboratory. Instead, our experiments are in the limit of low Mach  
155 number where compressibility effects are negligible.

156 Despite their low Mach number, the experiments reported here are in the limit where the impactor kinetic  
157 energy is large compared with viscous dissipation and interfacial energies ( $Re > 10^3$  and  $We > 5 \times 10^4$ ).  
158 Although these values are far from the values for planetary impacts (supplementary Table 1), they are  
159 among the highest reported for liquid impacts (Bisighini et al., 2010; Ray et al., 2015). This implies that  
160 in our experiments, and in planetary collisions, inertia and buoyancy forces govern the dynamics, and  
161 hence determine the mixing (Ellison and Turner, 1959; Landeau et al., 2014). The experimental results  
162 can therefore be described solely in terms of two dimensionless control parameters: the normalised excess  
163 density  $P$  and the impact Froude number  $Fr$ . The Froude numbers  $Fr$  in our experiments match those of  
164 planetary impactors with a radius  $\gtrsim 100$  km (supplementary Table 1).

### 165 3.3. Diagnostics

166 In each experiment, we measure the size of the impactor  $R$ , and the impact velocity  $U$ , from which we  
167 construct the impact Froude number  $Fr$ . From each frame before the impactor reaches the target, we locate  
168 the 2D centroid of the impactor. We fit the position of this centroid as a function of time with a quadratic  
169 polynomial. From this fit, we compute the velocity  $U$  at the time when the centroid intersects the surface of  
170 the target.

171 To quantify mixing between the dyed impactor and the target, we use the light-attenuation technique  
172 (Cenedese and Dalziel, 1998). As detailed in supplementary section S2, we measure the vertical position  $z$   
173 of the centre of mass of the dyed liquid and its characteristic volume  $\tilde{V}$  normalised by the impactor volume.  
174 From this dimensionless volume  $\tilde{V}$ , we define the equivalent spherical radius of the dyed liquid  $r = R \tilde{V}^{1/3}$ .

175 Uncertainties in  $U$ ,  $z$  and  $\tilde{V}$  are typically on the order of 5%, 5%, and 15%, respectively. Uncertainties  
176 in  $U$  mainly come from the retraction of the latex membrane that produces spurious liquid spray at the  
177 impactor surface. Uncertainties in  $z$  and  $\tilde{V}$  mainly come from light reflections and refractions by waves  
178 generated by the impact at the target surface.

## 179 4. Results

### 180 4.1. Experimental observations

181 In all our experiments, we observe two main stages. At early times, the impact process dominates the  
182 dynamics (Fig.2). At later times, buoyancy forces become important and the impactor sinks into the lighter  
183 target pool, forming the so-called turbulent thermal (Fig.3). Below, we describe these two stages.

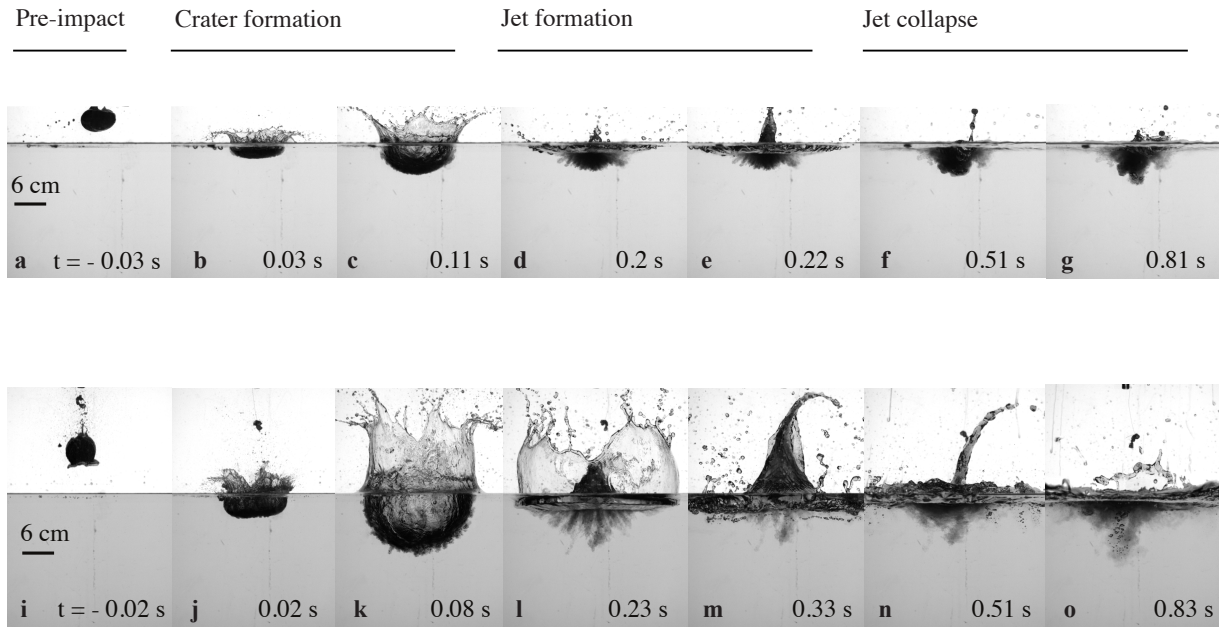


Figure 2: Early-time impact stage: impact cratering (b,c, and j,k), jet formation (d,e and l,m), jet collapse (f,g and n,o). First line: Low impact Froude number,  $Fr \approx 6$ ,  $U \approx 1.3 \text{ m s}^{-1}$ . Second line: High impact Froude number,  $Fr \approx 100$ ,  $U \approx 5.4 \text{ m s}^{-1}$ . In both experiments  $P \approx 0.02$  and the impactor radius  $R \approx 3 \text{ cm}$ . The experiments in the first and second lines correspond to supplementary movies S1 and S2, respectively.

#### 184 4.1.1. Short-time impact stage

185 The impact-dominated stage lasts about 1 s (Fig.2 and supplementary movies S1 and S2). We observe  
186 three successive processes in the impact stage.

187 The first process corresponds to the formation of a crater (Fig.2b,c and Fig.2j,k). The crater expands  
188 until its gravitational energy nearly matches the initial kinetic energy of the impactor (Pumphrey and El-  
189 more, 1990; Ray et al., 2015); at this point the crater reaches its maximum depth (Fig.2c and 2k). During the  
190 formation of the crater, we observe mushroom-shaped instabilities at the interface between the impactor and  
191 the target (Fig.4). These instabilities induce some mixing between the two fluids. We find that these struc-  
192 tures disappear in the absence of a density difference, i.e. for  $P = 0$ . We can understand these instabilities  
193 by considering the acceleration history of the fluids.

194 At the moment of impact, the impactor and target fluids are impulsively decelerated and accelerated,  
195 respectively. This impulsive acceleration can trigger the growth of perturbations through an incompress-  
196 ible Richtmyer-Meshkov mechanism (Jacobs and Sheeley, 1996; Lund and Dalziel, 2014). This growth is  
197 then modified during the opening of the crater. The crater floor decelerates until it reaches its maximum  
198 depth (Fig.2c,k). This deceleration, together with the gravitational acceleration, drives a Rayleigh-Taylor  
199 instability at the interface between the dense impactor and the lighter pool (Rayleigh, 1883).

200 The second process in the impact stage is the collapse of the crater because of gravity and the formation  
201 of a jet (Fig.2de and Fig.2lm). This jet is similar to that observed in drop impacts (Ghabache et al., 2014).

202 The jet eventually stops rising, marking the end of jet formation and the beginning of the jet collapse

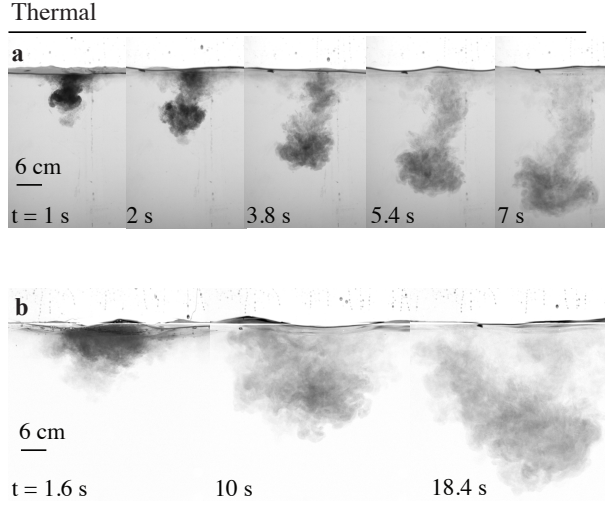


Figure 3: Late-time thermal stage following the impact shown in Fig.2. (a) Low impact Froude number,  $Fr \approx 6$ ,  $U \approx 1.3 \text{ m s}^{-1}$ . (b) High impact Froude number,  $Fr \approx 100$ ,  $U \approx 5.4 \text{ m s}^{-1}$ . In both experiments  $P \approx 0.02$  and the impactor radius  $R \approx 3 \text{ cm}$ . The experiments in (a) and (b) correspond to supplementary movies S1 and S2, respectively.

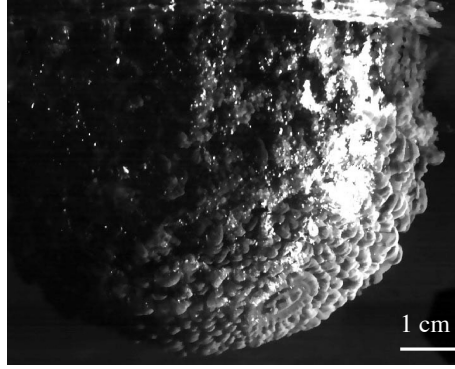


Figure 4: Mushroom-shaped structures observed during the crater opening process shown in Fig.2a,b,c and Fig.2i,j,k. In this experiment,  $Fr \approx 20$  and  $P \approx 0.18$ . To obtain this image we added fluorescein in the impacting liquid and we filmed the impact from below, illuminating it from the side with a halogen lamp.

203 process (Fig.2f and Fig.2n). The jet collapses under its own weight, accelerating the fluid it contains down-  
 204 wards and causing additional mixing between the impactor and the target.

205 The experiment shown in the first row of Fig.2 has  $Fr \approx 6$  (supplementary movie S1), while that in  
 206 the second row has  $Fr \approx 100$  (supplementary movie S2). We observe that the maximum crater depth, the  
 207 extent of the splash and the height of the secondary jet, all normalised by the impactor size, increase with  
 208 increasing impact Froude number.

#### 209 4.1.2. Long-time thermal stage

210 The denser impacting fluid eventually descends into the lighter target (Fig.3). This stage introduces  
 211 mixing over a much longer timescale, resulting from the total buoyancy of the impacting liquid in the  
 212 target. The impacting liquid forms a buoyant cloud that grows by entrainment of target liquid, the so-called  
 213 thermal (Taylor, 1945; Batchelor, 1954; Morton et al., 1956; Scorer, 1957).

214 Recently, several investigations used turbulent thermals to model core formation (Deguen et al., 2011,  
 215 2014; Landeau et al., 2014; Wacheul and Le Bars, 2018). However, these studies lack an initial impact stage:

216 the analogue fluid for the impactor core was initially immersed in the ambient and at rest. It is therefore  
 217 noteworthy that we recover a turbulent thermal in our impact experiments. Still, including the impact stage  
 218 is crucial: the extent of the thermal, and hence the mixing, is larger with  $Fr \simeq 100$  (Fig.3b) than with  $Fr \simeq 6$   
 219 (Fig.3a). The Froude number also affects the initial shape of the thermal, which is spherical with  $Fr \simeq 6$   
 220 (Fig.3a) but closer to a hemisphere with  $Fr \simeq 100$  (Fig.3b). This demonstrates that inertia, characterised by  
 221 the impact Froude number, significantly affects mixing between the impactor and the target.

#### 222 4.2. Crater depth scaling

Before quantifying mixing, we first compare the impacts from our experiments to those from the litera-  
 ture. Fig.5 shows the maximum crater depth in our experiments with  $P = 0$ . When  $P$  is fixed, the normalised  
 maximum crater depth  $H/R$  depends only on  $Fr$ . We find the following least squares best-fitting power-law

$$\frac{H}{R} = a_1 Fr^{a_2}, \quad (2)$$

223 where  $a_1 = 1.1 \pm 0.05$  and  $a_2 = 0.24 \pm 0.01$ , as shown as a solid line in Fig.5. Relation (2) is a  $\pi$ -group  
 224 scaling law (Melosh, 1989).

To understand the origin of (2), we assume that the kinetic energy of the impactor is converted com-  
 pletely into potential energy in a hemispherical crater of maximum depth  $H$ , so that

$$\frac{2}{3} \rho_i U^2 R^3 = \frac{1}{4} \rho_t g H^4, \quad (3)$$

where we neglect the density of air compared to  $\rho_i$  and  $\rho_t$ . Thus, the dimensionless crater depth,

$$\frac{H}{R} = \left(\frac{8}{3}\right)^{1/4} \left(\frac{\rho_i}{\rho_t}\right)^{1/4} Fr^{1/4}. \quad (4)$$

225 This energy scaling  $H/R \sim Fr^{1/4}$  is well-known for subsonic impacts of drops with a radius  $R < 3$  mm in  
 226 another liquid (Engel, 1967; Pumphrey and Elmore, 1990; Ray et al., 2015; Jain et al., 2019) and subsonic  
 227 impacts of solid spheres into granular materials (Walsh et al., 2003; Takita and Sumita, 2013; Seaton, 2006).

228 The experimental exponent  $a_2 = 0.24 \pm 0.01$  in (2) agrees well with the 1/4 theoretical prediction given  
 229 in (4). Even the prefactor  $a_1 = 1.1$  is close to the theoretical prediction  $(8/3)^{1/4} \simeq 1.28$  given in (4) for  
 230  $\rho_i = \rho_t$ . These results confirm that inertia and gravity are the two dominant forces in our experiments, while  
 231 viscous and surface tension forces play a secondary role. This is the relevant regime for large planetary  
 232 impacts.

233 Unlike our experiments, planetary impacts are supersonic. Previous investigations find an exponent  
 234  $a_2 \simeq 0.2$  for hypervelocity impacts, suggesting that the 1/4 power-law scaling (4) does not hold (Prieur  
 235 et al., 2017). Despite this difference in  $a_2$ , the crater depth in our experiments is within 14% of that predicted  
 236 by hypervelocity scalings (dotted line in Fig.5 and supplementary section S5).

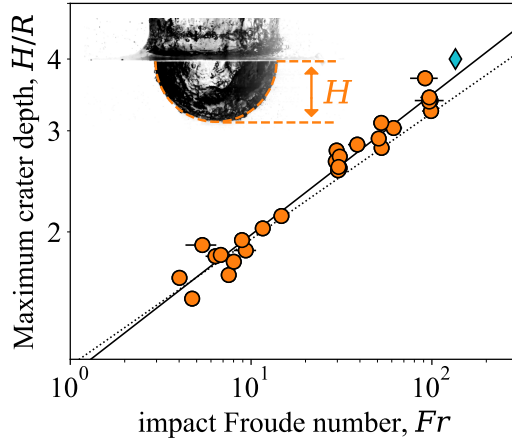


Figure 5: Maximum crater depth  $H$  normalised by the impactor radius  $R$  as a function of the impact Froude number  $Fr$ . The inset shows the depth  $H$  and the crater best-fit semi-circle (dashed yellow curve) in a given experiment; this illustrates that our experimental craters are close to hemispherical. The solid line is the least-square best fit scaling, given by  $H/R = a_1 Fr^{a_2}$ , where  $a_1 = 1.1 \pm 0.05$  and  $a_2 = 0.24 \pm 0.01$ . The dotted line is the scaling law  $H/R = 1.17 Fr^{0.22}$  obtained by Schmidt and Housen (1987) in experiments of solid projectiles into water at hypervelocities. We assume a hemispherical crater to convert their scalings for the crater radius into a scaling for the crater depth. In the experiments of Schmidt and Housen (1987), the Froude number ranges from  $Fr = 10^8$  to  $Fr = 3 \times 10^9$ . The dotted line is therefore an extrapolation over 6 orders of magnitude in  $Fr$ . The blue diamond is the maximum crater depth  $H/R \approx 4$  in an axisymmetric hypervelocity impact simulation of Kendall and Melosh (2016) for  $Fr \approx 135$  (see their figure 2b).

### 237 4.3. Mixing scaling

238 The mixing between the impactor and the target occurs both during the impact (Fig.2) and within the  
 239 resultant thermal (Fig.3). Here we determine power-law scalings for mixing, quantifying the dominant  
 240 processes during both the impact and thermal stage.

At late times, during the thermal stage (Fig.3), the mixing qualitatively agrees with the model of Deguen et al. (2011, 2014). This model describes the growth of the thermal as it falls downwards in the magma ocean. It is based on the turbulent entrainment hypothesis, developed by Taylor (1945) and Morton et al. (1956), and inspired by the work of Batchelor (1954). It assumes that the growth rate of the thermal is proportional to its velocity and surface area. This hypothesis implies that the growth of the thermal radius  $r$  is linear with the depth  $z$  of its centre of mass such that

$$r = r_0 + \alpha z, \quad (5)$$

241 where  $\alpha$  is called the entrainment coefficient and  $r_0$  the effective initial radius of the thermal at  $z = 0$  (Morton  
 242 et al., 1956).

243 As shown in Fig.6a, we recover the linear relation (5) in our experiments, as long as the depth of the  
 244 centre of mass is larger than about  $2R$ . This demonstrates that the turbulent entrainment model (5) accurately  
 245 describes mixing at long times in our liquid impacts.

246 The radius  $r$  in Fig.6 is based on summations over the entire image (supplementary section S2). Hence,  
 247  $r$  measures the extent of the structure formed by the thermal and its tail. Accounting for all our experiments,  
 248 we find that the entrainment coefficient for the thermal with its tail is  $\alpha = 0.6 \pm 0.1$ .

249 We also measure the half-width of the thermal (Bush et al., 2003), and the radius of the semi-axisymmetric

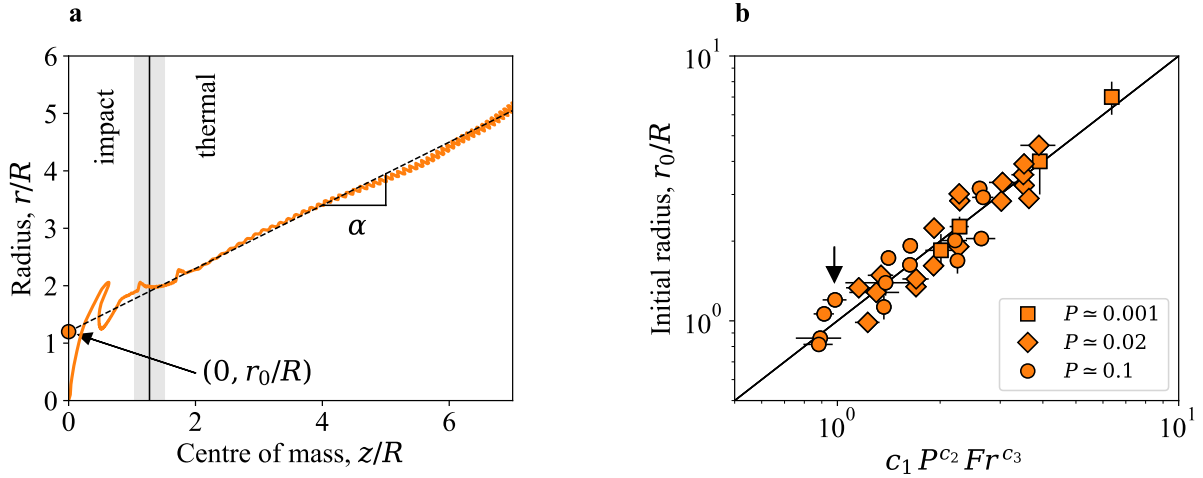


Figure 6: (a) Thermal radius  $r$  as a function of the depth of its centre of mass  $z$ , both normalised by  $R$ . In this experiment  $Fr \approx 8$  and  $P \approx 0.1$ . The dashed line is the least-square linear best-fit  $r/R = (r_0 + \alpha z)/R$ , with slope  $\alpha = 0.55$  and  $r_0/R \approx 1.2$ . The effective initial radius of the thermal,  $r_0$ , is defined as the value of the best-fit radius  $r$  for  $z = 0$ . The arrow denotes the point of coordinates  $(0, r_0/R)$ . The vertical grey region marks the transition from the early impact to the late thermal stage. (b) Initial radius of the thermal  $r_0$ , normalised by the impactor radius  $R$ , versus least-squares best-fit power-law scaling as a function of the normalised density excess  $P$  and the impact Froude number  $Fr$ . Squares:  $P \approx 0.001$ ; diamonds:  $P \approx 0.02$ ; circles:  $P \approx 0.1$ . The best-fit coefficients are:  $c_1 = 0.29 \pm 0.03$ ,  $c_2 = -0.19 \pm 0.03$ ,  $c_3 = 0.4 \pm 0.05$ . The arrow locates the experiment shown in (a). Error bars indicate measurement uncertainties.

250 reconstructed volume (Landeau et al., 2014). Although these quantities depend on an arbitrary binarization  
 251 threshold, they minimise the effect of the tail. With these definitions, we find an averaged entrainment co-  
 252 efficient of  $\alpha = 0.25 \pm 0.1$  for the thermal without its tail. This value is indistinguishable from that in pure  
 253 thermals (Scorer, 1957; Bush et al., 2003).

254 The large value of  $\alpha$  when including the tail is a geometric effect. The vertical extent of the structure is  
 255 then set by the height of the tail, which nearly equals to the distance  $z$  travelled by the thermal. This distance  
 256 grows faster than the width of the thermal, causing the large  $\alpha$  value. Note that the tail is not yet formed at  
 257 the beginning of the thermal stage, and hence, it does not affect the initial radius  $r_0$ . As the tail contains a  
 258 small fraction of the impactor mass, we use  $\alpha = 0.25$  in planetary applications.

Despite the agreement between our experiments and relation (5), an important difference with the model  
 of Deguen et al. (2011, 2014) arises. Deguen et al. (2011, 2014) assume that  $r_0$  is equal to the impactor core  
 radius and is independent from the impact velocity. In contrast, we observe that the impact Froude number,  
 and therefore the impact velocity, strongly affects the radius of the thermal at a given depth (Fig.3). To  
 quantify this, in each experiment, we fit relation (5) to the late-time radius to determine the effective initial  
 radius  $r_0$  of the thermal (Fig.6a). In Fig.6b, we show the dimensionless, effective initial radius,  $r_0/R$ , in all  
 our experiments as a function of the least-square best fit

$$\frac{r_0}{R} = c_1 P^{c_2} Fr^{c_3}, \quad (6)$$

259 where  $Fr$  is the impact Froude number and  $P$  the normalised excess density. We find  $c_1 = 0.29 \pm 0.03$ ,  
 260  $c_2 = -0.19 \pm 0.03$ ,  $c_3 = 0.4 \pm 0.05$ . The sign of the power-law exponent  $c_3$  agrees with the qualitative



261 observation drawn in section 4.1: that the extent of mixing during the impact stage increases with increasing  
262 impact Froude number. This trend is intuitive: the larger the impactor kinetic energy, the more mixing the  
263 impact produces.

264 The negative sign of the exponent  $c_2$  is more unexpected. It implies that the larger the excess density,  
265 the less mixing occurs at a given depth. As discussed before, the structures growing during crater opening  
266 (shown in Fig.4) are related to incompressible Richtmyer-Meshkov or Rayleigh-Taylor instabilities. At a  
267 fixed time, mixing by either of these mechanisms increases with the normalised excess density  $P$  (Dalziel  
268 et al., 1999; Holmes et al., 1999; Lund and Dalziel, 2014). This is at odds with the sign of  $c_2$ , suggesting  
269 that the instabilities shown in Fig.4 are not the dominant contribution to mixing.

270 Some degree of mixing could occur during the rise of the secondary jet (Fig.2d,e and Fig.2l,m). In this  
271 case, the extent of mixing, and hence  $r_0$ , should scale as the jet size. In previous work, the width and the  
272 height of the jet follow the same scaling, which we obtain by equating the gravitational energy in the jet to  
273 the kinetic energy of the impactor (Ghabache et al., 2014). With these assumptions, one obtains that the jet  
274 size evolves as  $Fr^{1/4}(\rho_i/\rho_{jet})^{1/4}$ , where  $\rho_{jet}$  is the jet mean density. Thus, if mixing occurs during the rise of  
275 the jet, we expect  $c_3 = 1/4$  and  $c_2 > 0$ . This again cannot explain the observed scaling.

276 Thus, the only remaining process that can account for scaling (6) is the collapse of the jet, and the  
277 subsequent dynamics, illustrated in Fig.2f,g and Fig.2n,o. In section 4.4, we develop a scaling analysis that  
278 suggests that jet collapse dominates mixing during giant impacts.

#### 279 4.4. *Mixing model*

280 In order to understand mixing between an impactor and a lighter target liquid, we first describe exper-  
281 iments with no excess density, i.e. with  $P = 0$ . In these, after the collapse of the jet, the impacting liquid  
282 remains near the surface of the target, but undergoes a slow lateral growth (supplementary Figure S4). This  
283 implies that, during the impact stage, the downward momentum of the jet is converted into lateral spreading  
284 of the impacting fluid. As the impacting liquid spreads, shear-generated turbulence mixes the impactor with  
285 the target. This mixing continues until the kinetic energy is entirely dissipated. In the absence of buoyancy,  
286 the impacting liquid never migrates downward as a thermal (supplementary Figure S4).

287 In contrast, when the impactor is more dense than the target, a buoyancy force arises as the jet releases  
288 the impacting liquid. Buoyancy generates a downward momentum. When this balances the momentum of  
289 the jet, the impactor stops spreading horizontally and descends as a thermal (Fig.3). For a given impact,  
290 the denser the impactor, the earlier it migrates downwards, and hence the smaller the mixing prior to the  
291 thermal stage. This rationale explains why the initial extent of the thermal  $r_0$  decreases as the excess density  
292  $P$  increases, as indicated by scaling (6).

We therefore hypothesise that the thermal starts descending when the buoyancy-induced momentum  
becomes larger than the momentum of the collapsing jet,  $M_{jet}$ . A scaling analysis suggests that this takes a

time

$$t_b \sim \frac{M_{jet}}{B}, \quad (7)$$

293 where  $B = \frac{4}{3}\pi R^3 P g$  is the total buoyancy of the impacting liquid. The time  $t_b$  corresponds to the transition  
 294 from the impact stage (Fig.2) to the thermal stage (Fig.3).

During the time  $t_b$ , the impacting liquid spreads horizontally over a distance

$$l_b \sim \sqrt{M_{jet}/B}^{1/4}. \quad (8)$$

295 The length  $l_b$  represents the distance, travelled horizontally, after which the momentum of the impactor is  
 296 dominated by buoyancy effects, at which point it sinks as a pure thermal. The length  $l_b$  is analogous to  
 297 the Morton length, which characterises the transition from forced to pure turbulent plumes (Morton, 1959).

298 Note that the Morton length is vertical while  $l_b$  is horizontal.

When  $P \ll 1$ , the maximum jet height  $H_{jet}$  and maximum jet volume scale as  $R Fr^{1/4}$  and  $R^3 Fr^{3/4}$ ,  
 respectively (Ghabache et al., 2014). We then assume that the speed of the collapsing jet scales as  $\sqrt{g H_{jet}}$   
 to obtain

$$M_{jet} \sim g^{1/2} H_{jet}^{7/2} \sim g^{1/2} R^{7/2} Fr^{7/8}. \quad (9)$$

299 Inserting (9) into (8) and (7), we obtain scalings for the dimensionless time,

$$\tilde{t}_b = t_b \sqrt{g/R} \sim P^{-1} Fr^{7/8}, \quad (10)$$

300 and dimensionless distance,

$$\tilde{l}_b = l_b / R \sim P^{-1/4} Fr^{7/16}. \quad (11)$$

301 Following the turbulent entrainment hypothesis (Morton et al., 1956), we assume that the radius of the  
 302 dyed region  $r_0$  scales as the distance travelled,  $l_b$ , times an entrainment coefficient  $\alpha$ . This implies that the  
 303 dimensionless volume of the dyed liquid

$$\tilde{V} = \frac{r_0^3}{R^3} \sim \alpha^3 P^{-3/4} Fr^{21/16}. \quad (12)$$

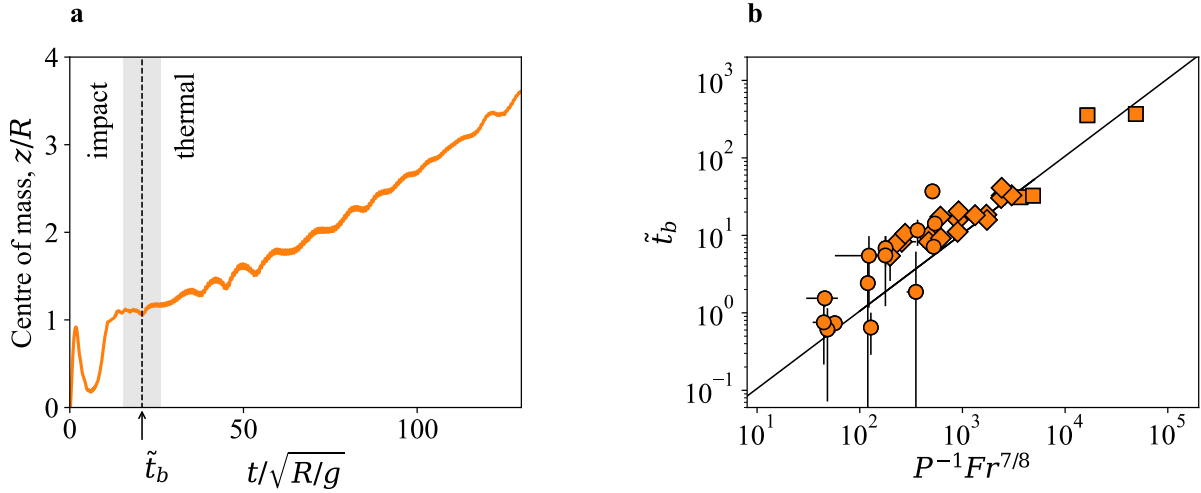


Figure 7: (a) Centre of mass of the dyed fluid, normalised by  $R$ , as a function of time, normalised by  $\sqrt{R/g}$  in a single experiment. The time  $\tilde{t}_b$  marks the end of the impact stage and the beginning of the thermal stage, in which the centre of mass increases monotonously with time. Oscillations are due to gravity waves on the free surface. (b) Time  $\tilde{t}_b$ , normalised by  $\sqrt{R/g}$ , measured in all experiments versus its theoretical evolution  $P^{-1} Fr^{7/8}$ . The solid curve is the least-square best-fit given by  $\tilde{t}_b = c_4 P^{-1} Fr^{7/8}$ , where  $c_4 = 0.010 \pm 0.003$  is the only fitted coefficient. Squares:  $P \approx 0.001$ ; diamonds:  $P \approx 0.02$ ; circles:  $P \approx 0.1$ .

Fig.7 shows that the experimentally-measured values of  $\tilde{t}_b$  agree with the model prediction (10). To test scaling (12), we now estimate the dimensionless thermal volume  $\tilde{V}$  (defined in supplementary section S2) at the thermal initiation time  $\tilde{t}_b$  in all our experiments. As shown in Fig.8, the thermal volume  $\tilde{V}$  at  $\tilde{t}_b$  agrees well with the model prediction from (12). We find the following experimental least-square best-fit

$$\tilde{V} = (0.019 \pm 0.003) P^{-3/4} Fr^{21/16}. \quad (13)$$

304 In turbulent shear flows, such as jets or shear layers, the entrainment coefficient is typically  $\alpha = 0.07 - 0.37$   
 305 (Carazzo et al., 2006; Slessor et al., 2000). This yields a prefactor  $\alpha^3$  in (12) in the range  $0.0003 - 0.05$ ,  
 306 which includes our best-fit prefactor  $0.019 \pm 0.003$ .

307 Taking (12) to the power  $1/3$ , we predict  $r_0/R \sim \alpha P^{-1/4} Fr^{7/16}$ , which corresponds to  $c_2 = -1/4$  and  
 308  $c_3 = 7/16 \approx 0.44$ . This predicted value of  $c_3$  is within the error bars of its experimentally-measured value  
 309 in (6). The predicted value  $c_2 = -1/4$  is negative, as the experimental value, but its magnitude is slightly  
 310 higher than the observation. This may be due to a small mixing contribution from the mushroom-shaped  
 311 instabilities that grow during crater opening (Fig.4).

## 312 5. Discussion

### 313 5.1. Comparison with impact simulations

314 In the simulations of Kendall and Melosh (2016), the opening of a crater stretches the impactor into a  
 315 lenticular volume. This also occurs in our experiments. However, we observe that the impactor spreads  
 316 over the entire crater floor (Fig. 2k), and not within an inner crater as in Kendall and Melosh (2016).

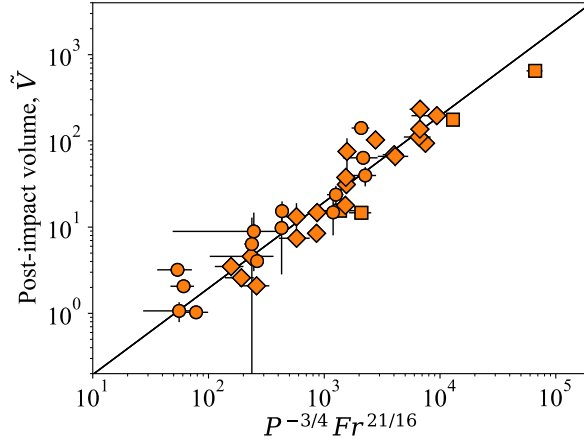


Figure 8: Measured post-impact volume of dyed fluid, normalised by the impactor volume, versus its theoretical evolution  $P^{-3/4} Fr^{21/16}$ . Squares:  $P \approx 0.001$ ; diamonds:  $P \approx 0.02$ ; circles:  $P \approx 0.1$ . Error bars indicate measurement uncertainties. In this figure, the volume of dyed fluid  $\tilde{V}$  is equal to  $(3 s_x)^2 3 s_z$ , where  $s_x$  and  $s_z$  are the second central moments of the concentration  $c(x, z)$  in the horizontal and vertical direction, respectively (supplementary section S2). The volume  $\tilde{V}$  is measured at time  $\tilde{t}_b$ , as defined in Fig.7a, marking the beginning of the buoyancy-driven stage shown in Fig. 3. The solid curve is the least-square best-fit given by  $\tilde{V} = c_5 P^{-3/4} Fr^{21/16}$ , where  $c_5 = 0.019 \pm 0.003$  is the only fitted coefficient.

317 In experiments, the impactor is always entrained by the central jet (Fig. 2m). This happens in the 3D  
 318 simulations of Kendall and Melosh (2016), but not in their 2D simulations.

319 In the vertical impact of Kendall and Melosh (2016), at impact speed  $U = 11.5 \text{ km s}^{-1}$ , the maximum  
 320 crater depth is  $\approx 400 \text{ km}$ , i.e.  $H \approx 4R$ . In this simulation,  $Fr \approx 135$  and  $P = (\rho_i - \rho_t) / \rho_t \approx 0.14$ , where  
 321  $\rho_i$  is the mean density of the impactor. This definition for  $P$  is supported by our results, which suggest that  
 322 mixing depends only on the jet momentum and the total buoyancy of the impactor (section 4.4). With this  
 323 Froude number, our scaling (2) predicts  $H \approx 3.7R$ , which deviates by only 7.5% from the numerical value  
 324 (Fig. 5). Incorporating the factor  $(\rho_i / \rho_t)^{1/4}$  from (4) into scaling (2), we predict  $H \approx 3.9R$ , which now  
 325 deviates by only 3%.

326 With  $P \approx 0.14$  and  $Fr \approx 135$ , our scaling (13) predicts a post-impact volume  $\tilde{V} \approx 51$  at time  $t_b \approx$   
 327  $500 \pm 200 \text{ s}$ . This means that the impactor core is dispersed within a volume 51 times the impactor. In  
 328 figure A.2 of Kendall and Melosh (2016), at a comparable time of 500 s, the vertical extent  $l_z \approx 1600 \text{ km}$   
 329 and horizontal extent  $l_x \approx 200 \text{ km}$ . Assuming a cylindrical structure, this leads to  $\tilde{V} \approx 3 (l_x^2 l_z) / 16 R^3 \approx 12$ .  
 330 At a slightly later time of 1000 s,  $l_z \approx 800 \text{ km}$  and  $l_x \approx 400 \text{ km}$  (figure 6 of Kendall and Melosh, 2016),  
 331 leading to  $\tilde{V} \approx 3 (l_x^2 l_z) / 16 R^3 \approx 24$ . These values for  $\tilde{V}$  are 2 to 4 times smaller than that predicted by our  
 332 scaling law, but they agree reasonably well when considering that  $\tilde{V}$  varies over 3 orders of magnitude in our  
 333 experiments (Fig.8). Furthermore, this 50% – 75% discrepancy in volume is only a 20% – 38% discrepancy  
 334 in radius.

335 These differences in mixing may come from compressibility, which is negligible in our experiments. In  
 336 simulations, compressibility effects are significant at the beginning of the opening of the crater. A fraction  
 337 of the impactor energy is then transported away by shock waves, and hence is not available for mixing.  
 338 Compressibility effects may be responsible for the inner crater, which limits the spreading of the impactor

339 core in the simulations of Kendall and Melosh (2016) (see their figure 2). At later times, as the crater  
340 expands, the impact kinetic energy is converted into potential energy and imparted to an increasing volume  
341 of target material. Thus, flow velocities rapidly decrease to subsonic speeds. In the supplementary movies  
342 of Kendall and Melosh (2016), the velocity of the metal is  $\lesssim 300 \text{ m s}^{-1}$  after the crater reaches its maximum  
343 size. Such speeds correspond to a low Mach number  $\sim 0.05 - 0.1$ . Compressibility is therefore unlikely  
344 to affect mixing after the cratering stage. Assuming compressibility is responsible for the differences in  
345 mixing, one needs to correct our predictions by a factor of 0.25 to 0.5 in  $\tilde{V}$ , and hence 0.6 to 0.8 in  $r_0$ .

346 The lower level of mixing in simulations might also originate from a lower level of turbulence. Our  
347 predictions would then need no correction factor. Despite the high resolution used by Kendall and Melosh  
348 (2016), the grid size, which ranges from 2.5 to 10 km, is much larger than the smallest turbulent scale  
349  $RRe^{-3/4} \lesssim 0.1 \text{ mm}$  (caption in supplementary Table 1). This explains why the mixing increases with  
350 decreasing grid size in simulations (supplementary figures A1 and A3 in Kendall and Melosh, 2016). For  
351 example, the post-impact volume  $\tilde{V}$  at time 500 s is multiplied by  $\sim 2$  when decreasing the grid size from  
352 5 to 2.5 km. From these observations, Kendall & Melosh predict a larger level of mixing when reaching a  
353 more turbulent regime. This agrees with our experimental scalings.

354 Finally, our experiments model the impactor as a single phase, while it is differentiated into a core and  
355 a mantle in the simulations of Kendall and Melosh (2016). In supplementary section S6, we show that the  
356 jet likely entrains the core of a differentiated impactor during crater collapse. With this assumption, mixing  
357 depends only on the total buoyancy and momentum of the collapsing jet, as inferred in section 4.4. These  
358 quantities do not depend on the mass distribution in the impactor. We therefore expect our scaling laws to  
359 hold for differentiated impactors.

## 360 5.2. Implications for metal-silicate mixing

361 In our experiments, we observe two main stages. At early times, the impact controls the dynamics.  
362 The impactor opens a crater, which collapses into an upward jet (Fig.2); the jet stops and collapses due to  
363 gravity, releasing the denser impacting liquid. At late times, the impacting liquid descends into the target as  
364 a turbulent thermal (Fig.3). The late thermal stage is similar to that observed in previous investigations that  
365 neglect the impact process (Deguen et al., 2011, 2014).

366 However, Deguen et al. (2011, 2014) assumed that the initial thermal volume is equal to the volume  
367 of the impactor core and is independent of the impact velocity. In contrast, we find that increasing the  
368 impact velocity strongly increases the initial thermal volume (Fig.3). We found that the volume of mixed  
369 target, which is an analogue for the equilibrated silicates, increases with increasing impact Froude number  
370  $Fr = U^2/gR$  (Fig.6 and Fig.8, and scalings (6) and (13)). We now translate these results into parameters  
371 that can be used in geochemical models of Earth's accretion.

Applied to planetary impacts, the impact Froude number is the ratio of the kinetic energy to the gravita-

tional potential energy at impact, given by

$$Fr = \frac{U^2}{RG(M + M_t)/(R + R_t)^2} = 2 \left(1 + \frac{R_t}{R}\right) \frac{U^2}{U_e^2}, \quad (14)$$

372 where  $U$  is the impact velocity,  $U_e = \sqrt{2G(M + M_t)/(R + R_t)}$  the mutual escape velocity,  $G$  the gravitational  
 373 constant,  $R$  and  $R_t$  are the impactor and target radius, and  $M$  and  $M_t$ , the mass of the impactor and target  
 374 planet, respectively. During Earth's accretion, the impact velocity is usually one to three times the escape  
 375 velocity (Agnor et al., 1999). Thus, the impact Froude number scales as  $(1 + R_t/R)$ . This number is on the  
 376 order of unity for a giant impact, but it is much larger than unity for a small impactor of less than about 100  
 377 km in radius. Since mixing increases with the Froude number (Fig.8), this implies that small, low-energy  
 378 impacts generate much more mixing, relative to their size, than giant impacts.

To quantify this dependence of mixing on the impactor size, we now derive the amount of silicates  
 entrained in the thermal. Our experimental scaling (6) for the initial volume of the thermal relates the  
 initial thermal radius,  $r_0$ , to the impact Froude number,  $Fr$ , and the dimensionless excess density,  $P$ . Using  
 expression (14) for  $Fr$ , this scaling then becomes

$$\frac{r_0}{R} = c_1 2^{c_3} f_m^{c_2} \left(\frac{\rho_m - \rho_s}{\rho_s}\right)^{c_2} \left(\frac{U}{U_e}\right)^{2c_3} \left(1 + \frac{R_t}{R}\right)^{c_3}, \quad (15)$$

379 where  $c_1 = 0.29 \pm 0.03$ ,  $c_2 = -0.19 \pm 0.03$ ,  $c_3 = 0.4 \pm 0.05$  are experimental constants,  $\rho_m$  the density of  
 380 metal,  $\rho_s$  the density of silicates and  $f_m$  the initial volume fraction of metal in the impactor. We define  $P =$   
 381  $(\bar{\rho} - \rho_s) / \rho_s$ , as the normalised difference between the mean density of the impactor  $\bar{\rho} = f_m \rho_m + (1 - f_m) \rho_s$   
 382 and the silicate density.

Following the results of Deguen et al. (2014), we assume that the silicates entrained in the thermal  
 efficiently equilibrate with the impactor metal. We define the dimensionless mass of equilibrated silicates  
 $\Delta = M_s/M_m$ , where  $M_s$  is the mass of entrained silicates, and  $M_m$  the impactor core mass. In the aftermath  
 of the impact, just before the thermal descends into the magma ocean,  $\Delta$  takes the value

$$\Delta_0 = \frac{\rho_s}{\rho_m} \left[ \frac{1}{f_m} \left(\frac{r_0}{R}\right)^3 - 1 \right], \quad (16)$$

383 where, as before,  $r_0$  is the effective initial radius of the thermal. Inserting scaling (15) for  $r_0$  into (16), we  
 384 compute the normalised mass of silicates  $\Delta_0$ , mixed with metal by the impact stage, prior to its descent in  
 385 the magma ocean, as a function of the impact velocity, the impactor size and its volumetric metal fraction.

386 Fig.9a shows  $\Delta_0$  as a function of the impactor size. The mass of mixed silicates monotonically increases  
 387 with the impact velocity and the radius of the target relative to that of the impactor. For a small impact with  
 388 a 100 km-sized body at escape velocity, the impactor core mixes with 168 times its mass (circle in Fig.9a).  
 389 In contrast, a giant impact with a Mars-sized impactor, similar to the canonical Moon-forming scenario

390 (Canup, 2004), generates little mixing with a mass of mixed silicates less than 1.5 times the impactor core  
 391 (diamond in Fig.9a).

392 Fig.9a illustrates that mixing by giant impacts is highly sensitive to the impact speed and impactor size.  
 393 Another Moon-forming scenario is the impact of a high-speed sub-Mars object on a fast-spinning Earth  
 394 (Ćuk and Stewart, 2012). For this scenario, we predict that the impactor core mixes with 12 times its mass  
 395 of silicates (square in Fig.9a), more than 8 times the mass predicted for the canonical scenario (diamond).  
 396 This is counter-intuitive as the total kinetic energy of the impactor in Ćuk and Stewart (2012)'s scenario is 5  
 397 times less than in the canonical scenario. This scenario involves a smaller impactor at higher speed, which  
 398 therefore corresponds to a larger impact Froude number according to (14), forcing more efficient mixing.

In the previous paragraphs, we discussed the efficiency of mixing by the impact stage, when the metal  
 is at the top of the magma ocean. However, geochemical data record the end result of mixing, when the  
 thermal reaches the bottom of the ocean. To predict this final mixing, we use the effective initial radius  $r_0$   
 of the thermal in the aftermath of an impact, as predicted by our scaling (15), as the new initial condition  
 for the growth of the thermal radius in the ocean (Deguen et al., 2011)

$$r = r_0 + \alpha z, \quad (17)$$

where  $z$  the depth in the magma ocean and  $\alpha$  the entrainment coefficient. The mass of equilibrated silicates  
 at the bottom of the magma ocean, normalised by the impactor core mass, is then

$$\Delta = \frac{\rho_s}{\rho_m} \left[ \frac{1}{f_m} \left( \frac{r_0}{R} + \alpha \frac{z_{mo}}{R} \right)^3 - 1 \right], \quad (18)$$

399 where  $z_{mo}$  is the total depth of the magma ocean. We use (15) and (18) to estimate  $\Delta$  for a given impact,  
 400 knowing the impact velocity, the impactor size and the metal fraction of the impactor.

401 Fig.9b shows the mass of mixed silicates predicted by (18), assuming that the magma ocean is 30% of  
 402 the depth of the mantle. At the base of the magma ocean, we again predict more efficient mixing for small  
 403 impacts (circle) than for giant impacts (diamond and square). The three curves indicate a strong effect of  
 404 the impact speed. Fig.9c shows that the total mass of mixed silicates, when we include the mixing by the  
 405 impact process, is up to 100 times larger than the previous estimates of Deguen et al. (2011, 2014).

We define the degree of chemical equilibration,  $\mathcal{E}$ , for a given chemical element, as the mass exchanged  
 between metal and silicates to the maximum exchanged mass if the metal equilibrates with an infinite  
 volume of silicates. From mass conservation equations, Deguen et al. (2014) showed that

$$\mathcal{E} = \frac{k}{1 + D/\Delta}, \quad (19)$$

406 where  $k$  is the fraction of equilibrated metal,  $D$  is the metal-silicate partition coefficient. With this definition,

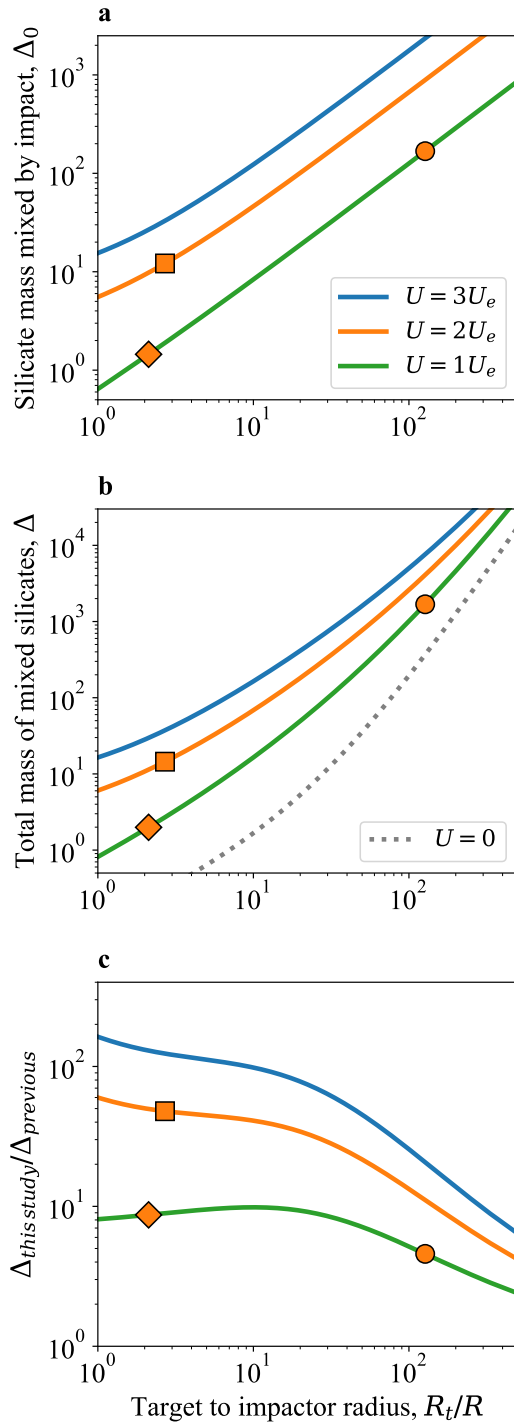


Figure 9: Mass of silicates mixed with metal by the impact stage  $\Delta_0$ , prior to the descent into the magma ocean (a), and by the impact and thermal stage at the bottom of the magma ocean  $\Delta$  (b), as a function of the target to impactor radius  $R_t/R$ . The silicate mass is normalised by the mass of impactor core. (c) Total mass of mixed silicates  $\Delta$  at the bottom of the magma ocean as predicted by our scalings that include the impact stage, divided by  $\Delta$  computed from the model of Deguen et al. (2014), as a function of the target to impactor radius  $R_t/R$ . Green: impact velocity  $U$  equals to the mutual escape velocity  $U_e$ . Orange:  $U = 2U_e$ . Blue:  $U = 3U_e$ . Grey dotted: model of Deguen et al. (2014) with no impact stage. Circle: impactor of 100 km in radius onto an Earth-sized target. Diamond: canonical Moon-forming scenario with a Mars-sized impactor (Canup, 2004). Square: Moon-forming scenario with an impactor mass 20 times smaller than the target onto a fast-spinning Earth (Ćuk and Stewart, 2012). We use relations (16) and (15) to compute  $\Delta_0$  and  $\Delta$ , taking  $f_m = 0.16$ ,  $(\rho_m - \rho_s)/\rho_s = 1$ ,  $\alpha = 0.25$  and assuming the magma ocean depth is 30% the mantle depth.

407 the limit  $\mathcal{E} = 0$  corresponds to no chemical transfer while  $\mathcal{E} = 1$  to full equilibration. As detailed in Deguen  
 408 et al. (2014), the degree of equilibration  $\mathcal{E}$  is a generalisation of the equilibrated metal fraction,  $k$  (Rudge



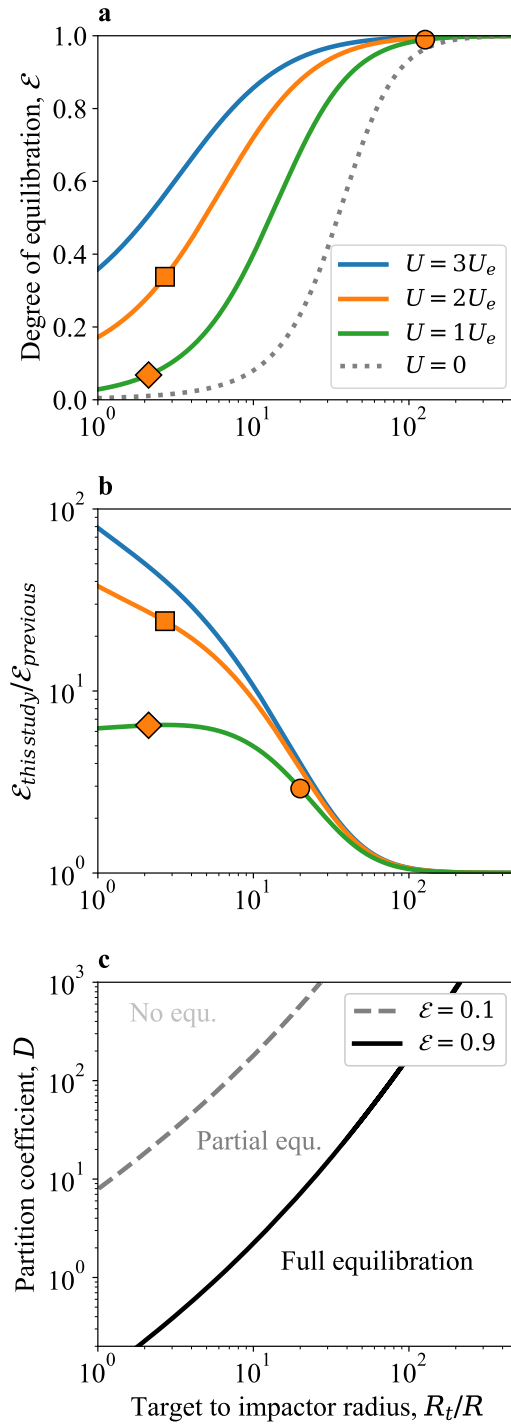


Figure 10: (a) Degree of equilibration  $\mathcal{E}$  at the bottom of the magma ocean as a function of the target to impactor radius  $R_t/R$  using relations (18) and (19), and taking a partition coefficient of 30 and  $\alpha = 0.25$ . Green:  $U = U_e$ . Orange:  $U = 2U_e$ . Blue:  $U = 3U_e$ . Grey dotted: model of Deguen et al. (2014) with no impact stage. Circle: impactor of 100 km in radius onto an Earth-sized target at  $U = U_e$ . Diamond: canonical Moon-forming scenario with a Mars-sized impactor (Canup, 2004). Square: Moon-forming scenario of Āuk and Stewart (2012). (b) Ratio of the degree of equilibration  $\mathcal{E}$  predicted by our scalings that include the impact stage to the degree of equilibration predicted by the model of Deguen et al. (2014). (c) Regime diagram for metal-silicate equilibration as a function of the target to impactor radius  $R_t/R$  and the partition coefficient  $D$ , with  $U = U_e$ . For all panels, we take  $f_m = 0.16$ ,  $(\rho_m - \rho_s)/\rho_s = 1$ ,  $k = 1$  and we assume that the depth of the magma ocean is 40% that of the mantle (Siebert et al., 2012; Fischer et al., 2015).

409 et al., 2010).

410 Fig.10a illustrates our prediction for the degree of equilibration when using (15) and (18). We assume  
 411  $k = 1$ , as suggested by Deguen et al. (2014), and choose  $D = 30$ . Fig.10a shows that we expect full

412 equilibration for small impactors with radii less than about 1/30 that of the target. For an Earth-sized target,  
413 this corresponds to impactors smaller than about 200 km. In contrast, the extent of equilibration is highly  
414 variable and very sensitive to the impact speed for giant collisions. For the Mars-sized impactor of the  
415 canonical Moon-forming scenario (diamond), the degree of equilibration  $\mathcal{E}$  is 0.07 while it is 0.34 for the  
416 Mercury-sized impactor proposed by Čuk and Stewart (2012) (square).

417 As shown in Fig.10b, the degree of equilibration predicted by our scalings is up to 20 times larger than  
418 previous estimates that neglect the effect of the impact speed. We therefore anticipate that our new scalings  
419 for metal-silicate mixing will strongly affect geochemical models of Earth’s formation (Rubie et al., 2015;  
420 Badro et al., 2018). They will also affect the timing of core formation, which is deduced from extinct  
421 radioactivity (Rudge et al., 2010). To illustrate this, we consider impactors at escape velocity with a radius  
422 30 times smaller than that of the proto-Earth. Our scalings predict that the mean degree of equilibration  
423 increases from 0.4 to 0.8 for these impacts (Fig.10ab). According to Figure 3b of Rudge et al. (2010), the  
424 duration of core formation from the Hf-W systematics is about 30 Myr for an equilibration  $\mathcal{E} = 0.8$ , but it  
425 is hardly constrained for  $\mathcal{E} = 0.4$  and could range from fifty to several hundred million years.

426 Similarly, the depth of the magma ocean deduced from siderophile elements depends on the assumed  
427 degree of equilibration. For impactors with a radius 20 times smaller than the target, the value of  $\mathcal{E}$ , which  
428 was close to 0.2 with previous models, is now in the range 0.7 – 0.95 (Fig.10ab). With such an increase,  
429 figure 7 from Fischer et al. (2017) predicts that the depth of the magma ocean decreases by up to 43%.

430 By definition, the degree of equilibration depends on the partition coefficient between metal and sili-  
431 cates, and therefore on the chemical element. This is illustrated in Fig.10c. For a metal-silicate partition  
432 coefficient  $D \lesssim 0.2$ , we predict full equilibration with  $\mathcal{E} > 0.9$  for most impacts, except for giant impactors  
433 larger than half the target in radius. In contrast, for  $D = 100$ , partial equilibration is the norm.

434 In conclusion, we found that mixing primarily depends on the impact Froude number, which measures  
435 the importance of the impactor kinetic energy to its gravitational energy. Applied to Earth’s formation, our  
436 scalings relate the mass of silicates entrained with metal as a function of the impact velocity, the impactor  
437 size and the depth of the magma ocean. We predict that the impact stage is responsible for up to 94%  
438 of the total mixing at the base of the magma ocean. This impact-induced mixing was entirely neglected  
439 in previous studies. Its effects on chemical transfers and geochemical models of core formation therefore  
440 deserves future investigations.

## 441 **Acknowledgements**

442 We are grateful to the late H. Jay Melosh and an anonymous reviewer for their valuable comments that  
443 significantly improved this manuscript. We thank Peter Olson, Miki Nakajima, H el ene de Maleprade, Paul  
444 Jarvis, Amy Bonsor, Kai W unnemann and Merlin Etzold for fruitful discussions at key moments during  
445 this project. We are extremely grateful to David Page-Croft, Colin Hitch, Jamie Partridge, John Milton, and

446 Mark Hallworth for their valuable help in setting up the experimental and visualization techniques. This  
447 project has received funding from the European Union's Horizon 2020 research and innovation program  
448 under the Marie Skłodowska-Curie Grant Agreement 703767. This work was also supported by the Pro-  
449 gramme National de Planétologie (PNP) of CNRS-INSU co-funded by CNES. RD and VL have received  
450 funding from the European Research Council (ERC) under the European Unions Horizon 2020 research and  
451 innovation programme (grant agreement 716429). This study contributes to the IdEx Université de Paris  
452 ANR-18-IDEX-0001.

### 453 **Author contributions**

454 ML, RD, DP, JN, SD contributed to the conception of the laboratory experiments and the measurement  
455 techniques. ML and DP conducted the experiments and analysed the data. All co-authors participated to  
456 the interpretation of data. ML wrote the paper; all co-authors carefully revised the manuscript and approved  
457 the final version.

### 458 **Declaration of interests**

459 The authors declare that they have no known competing financial interests or personal relationships that  
460 could have appeared to influence the work reported in this paper.

### 461 **References**

- 462 Agnor, C. B., Canup, R. M., Levison, H. F., 1999. On the character and consequences of large impacts in the late stage of terrestrial  
463 planet formation. *Icarus* 142 (1), 219–237.
- 464 Badro, J., Aubert, J., Hirose, K., Nomura, R., Blanchard, I., Borensztajn, S., Siebert, J., 2018. Magnesium partitioning between earth's  
465 mantle and core and its potential to drive an early exsolution geodynamo. *Geophys. Res. Lett.* 45 (24), 13–240.
- 466 Batchelor, G. K., 1954. Heat convection and buoyancy effects in fluids. *Quart. J. Roy. Met. Soc.* 80 (345), 339–358.
- 467 Bercovici, D., Ricard, Y., 2014. Plate tectonics, damage and inheritance. *Nature* 508 (7497), 513–516.
- 468 Bisighini, A., Cossali, G., Tropea, C., Roisman, I., 2010. Crater evolution after the impact of a drop onto a semi-infinite liquid target.  
469 *Physical Review E* 82 (3), 036319.
- 470 Blau, P., Axon, H., Goldstein, J., 1973. Investigation of the canyon diablo metallic spheroids and their relationship to the breakup of  
471 the canyon diablo meteorite. *J. Geophys. Res.* 78 (2), 363–374.
- 472 Bush, J. W. M., Thurber, B. A., Blanchette, F., 2003. Particle clouds in homogeneous and stratified environments. *J. Fluid Mech.* 489,  
473 29–54.
- 474 Canup, R. M., 2004. Simulations of a late lunar-forming impact. *Icarus* 168 (2), 433–456.
- 475 Carazzo, G., Kaminski, E., Tait, S., 2006. The route to self-similarity in turbulent jets and plumes. *J. Fluid Mech.* 547, 137.
- 476 Cenedese, C., Dalziel, S. B., 1998. Concentration and depth fields determined by the light transmitted through a dyed solution.  
477 *Proceedings of the 8th International Symposium on FlowVisualization* 8, 1–37.
- 478 Chambers, J. E., 2004. Planetary accretion in the inner Solar System. *Earth Planet. Sci. Lett.* 223 (3-4), 241–252.
- 479 Čuk, M., Stewart, S., 2012. Making the moon from a fast-spinning earth: a giant impact followed by resonant despinning. *Science*  
480 338 (6110), 1047–1052.

481 Dahl, T. W., Stevenson, D. J., 2010. Turbulent mixing of metal and silicate during planet accretion - And interpretation of the Hf-W  
482 chronometer. *Earth Plan. Sci. Lett.* 295 (1-2), 177–186.

483 Dalziel, S. B., Linden, P. F., Youngs, D. L., 1999. Self-similarity and internal structure of turbulence induced by Rayleigh-Taylor  
484 instability. *J. Fluid Mech.* 399, 1–48.

485 Deguen, R., Landeau, M., Olson, P., 2014. Turbulent metal-silicate mixing, fragmentation, and equilibration in magma oceans. *Earth  
486 Planet. Sci. Lett.* 391, 274–287.

487 Deguen, R., Olson, P., Cardin, P., 2011. Experiments on turbulent metal-silicate mixing in a magma ocean. *Earth and Planetary Science  
488 Letters* 310 (3-4), 303–313.

489 Ellison, T., Turner, J., 1959. Turbulent entrainment in stratified flows. *J. Fluid Mech.* 6 (03), 423–448.

490 Engel, O., 1967. Initial pressure, initial flow velocity, and the time dependence of crater depth in fluid impacts. *Journal of applied  
491 physics* 38 (10), 3935–3940.

492 Fischer, R., Campbell, A., Ciesla, F., 2017. Sensitivities of earth's core and mantle compositions to accretion and differentiation  
493 processes. *Earth Planet. Sci. Lett.* 458, 252–262.

494 Fischer, R., Nakajima, Y., Campbell, A., Frost, D., Harries, D., Langenhorst, F., Miyajima, N., Pollok, K., Rubie, D., 2015. High  
495 pressure metal-silicate partitioning of Ni, Co, V, Cr, Si, and O. *Geochem. Cosmochim. Acta* 167, 177–194.

496 Ghabache, É., Séon, T., Antkowiak, A., 2014. Liquid jet eruption from hollow relaxation. *J. Fluid Mech.* 761, 206–219.

497 Holmes, R., Dimonte, G., Fryxell, B., Gittings, M., Grove, J., Schneider, M., Sharp, D., Velikovich, A., Weaver, R., Zhang, Q., 1999.  
498 Richtmyer-Meshkov instability growth: experiment, simulation and theory. *J. Fluid Mech.* 389, 55–79.

499 Ichikawa, H., Labrosse, S., Kurita, K., 2010. Direct numerical simulation of an iron rain in the magma ocean. *J. Geophys. Res.* 115,  
500 doi:10.1029/2009JB006427.

501 Jacobs, J., Sheeley, J., 1996. Experimental study of incompressible richtmyer–meshkov instability. *Physics of Fluids* 8 (2), 405–415.

502 Jain, U., Jalaal, M., Lohse, D., Van Der Meer, D., 2019. Deep pool water-impacts of viscous oil droplets. *Soft matter* 15, 4629–4638.

503 Kendall, J., Melosh, H., 2016. Differentiated planetesimal impacts into a terrestrial magma ocean: Fate of the iron core. *Earth Planet.  
504 Sci. Lett.* 448, 24–33.

505 Kleine, T., Munker, C., Mezger, K., Palme, H., 2002. Rapid accretion and early core formation on asteroids and the terrestrial planets  
506 from Hf-W chronometry. *Nature* 418 (6901), 952–955.

507 Landeau, M., Deguen, R., Olson, P., 2014. Experiments on the fragmentation of a buoyant liquid volume in another liquid. *J. Fluid  
508 Mech.* 749, 478–518.

509 Lherm, V., Deguen, R., 2018. Small-scale metal/silicate equilibration during core formation: The influence of stretching enhanced  
510 diffusion on mixing. *J. Geophys. Res.* 123 (12), 10–496.

511 Lund, H. M., Dalziel, S. B., 2014. Bursting water balloons. *J. Fluid Mech.* 756, 771–815.

512 Maas, C., Manske, L., Wünnemann, K., Hansen, U., 2021. On the fate of impact-delivered metal in a terrestrial magma ocean. *Earth  
513 Plan. Sci. Lett.* 554, doi: 10.1016/j.epsl.2020.116680.

514 Melosh, H. J., 1990. Giant impacts and the thermal state of the early earth. In: Newsom, H., Jones, J. (Eds.), *Origin of the Earth.*  
515 Oxford University Press Inc.

516 Melosh, J., 1989. *Impact Cratering: A Geologic Process.* Oxford University Press Inc.

517 Morton, B. R., 1959. Forced plumes. *J. Fluid Mech.* 5 (1), 151–163.

518 Morton, B. R., Taylor, G., Turner, J. S., 1956. Turbulent gravitational convection from maintained and instantaneous sources. *Proc. R.  
519 Soc. Lond.* 234 (1196), 1–23.

520 Nakajima, M., Golabek, G., Wünnemann, K., Rubie, D., Burger, C., Melosh, H. J., Jacobson, S., Manske, L., Hull, S., 2020. Scaling  
521 laws for the geometry of an impact-induced magma ocean. *arXiv, submitted to Earth Planet. Sci. Lett.*, 2004.04269.

522 Olson, P., Deguen, R., Rudolph, M., Zhong, S., 2015. Core evolution driven by mantle global circulation. *Phys. Earth Planet. Int.* 243,  
523 44–55.

524 Patterson, C., Tilton, G., Inghram, M., 1955. Age of the earth. *Science* 121 (3134), 69–75.

525 Prieur, N., Rolf, T., Luther, R., Wünnemann, K., Xiao, Z., Werner, S., 2017. The effect of target properties on transient crater scaling  
526 for simple craters. *J. Geophys. Res.-Planets* 122 (8), 1704–1726.

527 Pumphrey, H., Elmore, P., 1990. The entrainment of bubbles by drop impacts. *J. Fluid Mech.* 220, 539–567.

528 Qaddah, B., Monteux, J., Clesi, V., Bouhifd, M., Le Bars, M., 2019. Dynamics and stability of an iron drop falling in a magma ocean.  
529 *Phys. Earth Planet. Int.* 289, 75–89.

530 Ray, B., Biswas, G., Sharma, A., 2015. Regimes during liquid drop impact on a liquid pool. *J. Fluid Mech.* 768, 492–523.

531 Rayleigh, L., 1883. Investigation of the character of the equilibrium of an incompressible heavy fluid of variable density. *Proc. Lond.*  
532 *Math. Soc.* 14, 70–177.

533 Ricard, Y., Sramek, O., Dubuffet, F., 2009. A multi-phase model of runaway core-mantle segregation in planetary embryos. *Earth*  
534 *Planet. Sci. Lett.* 284 (1-2), 144–150.

535 Rubie, D., Jacobson, S., Morbidelli, A., O'Brien, D., Young, E., de Vries, J., Nimmo, F., Palme, H., Frost, D., 2015. Accretion and  
536 differentiation of the terrestrial planets with implications for the compositions of early-formed solar system bodies and accretion of  
537 water. *Icarus* 248, 89–108.

538 Rubie, D. C., Melosh, H. J., Reid, J. E., Liebske, C., Richter, K., 2003. Mechanisms of metal-silicate equilibration in the terrestrial  
539 magma ocean. *Earth Planet. Sci. Lett.* 205 (3-4), 239–255.

540 Rudge, J. F., Kleine, T., Bourdon, B., 2010. Broad bounds on Earth's accretion and core formation constrained by geochemical models.  
541 *Nat. Geosci.* 3 (6), 439–443.

542 Samuel, H., 2012. A re-evaluation of metal diapir breakup and equilibration in terrestrial magma oceans. *Earth Planet. Sci. Lett.* 313,  
543 105–114.

544 Schmidt, R., Housen, K., 1987. Some recent advances in the scaling of impact and explosion cratering. *International Journal of Impact*  
545 *Engineering* 5 (1-4), 543–560.

546 Scorer, R. S., 1957. Experiments on convection of isolated masses of buoyant fluid. *J. Fluid Mech.* 2 (6), 583–594.

547 Seaton, M., 2006. Phd thesis: Particle resuspension by liquid droplets. DAMTP, University of Cambridge.

548 Siebert, J., Badro, J., Antonangeli, D., Ryerson, F., 2012. Metal–silicate partitioning of ni and co in a deep magma ocean. *Earth and*  
549 *Planet. Sci. Lett.* 321-322, 189–197.

550 Slessor, M., Zhuang, M., Dimotakis, P., 2000. Turbulent shear-layer mixing: growth-rate compressibility scaling. *J. Fluid Mech.* 414,  
551 35–45.

552 Takita, H., Sumita, I., 2013. Low-velocity impact cratering experiments in a wet sand target. *Physical Review E* 88 (2), 022203.

553 Taylor, G. I., 1945. Dynamics of a hot mass rising in air. U.S. Atomic Energy Commission, MDDC-919, LADC-276.

554 Tonks, W. B., Melosh, H. J., 1993. Magma ocean formation due to giant impacts. *J. Geophys. Res.* 98 (E3), 5319–5333.

555 Ulvrová, M., Coltice, N., Ricard, Y., Labrosse, S., Dubuffet, F., Velínský, J., Sramek, O., 2011. Compositional and thermal equilibra-  
556 tion of particles, drops, and diapirs in geophysical flows. *Geochem. Geophys. Geosystems.* 12 (10).

557 Vdovykin, G., 1973. The canyon diablo meteorite. *Space Science Reviews* 14 (6), 758–831.

558 Wacheul, J.-B., Le Bars, M., 2018. Experiments on fragmentation and thermo-chemical exchanges during planetary core formation.  
559 *Phys. Earth Planet. Int.* 276, 134–144.

560 Walsh, A., Holloway, K., Habdas, P., de Bruyn, J., 2003. Morphology and scaling of impact craters in granular media. *Physical review*  
561 *letters* 91 (10), 104301.

562 Worthington, A. M., 1908. A study of splashes. Longmans, Green, and Company.